

A Method for Lower Back Motion Assessment Using Wearable 6D Inertial Sensors

Marco Molnar^{*}, Manon Kok[†], Tilman Engel[‡], Hannes Kaplick[‡], Frank Mayer[‡] and Thomas Seel^{*}

^{*}Technische Universität Berlin, 10623 Berlin, Germany

[†]Delft University of Technology, 2628 CD Delft, the Netherlands

[‡]University of Potsdam, 14469, Potsdam, Germany

Abstract—Low back pain (LBP) is a leading cause of activity limitation. Objective assessment of the spinal motion plays a key role in diagnosis and treatment of LBP. We propose a method that facilitates clinical assessment of lower back motions by means of a wireless inertial sensor network. The sensor units are attached to the right and left side of the lumbar region, the pelvis and the thighs, respectively. Since magnetometers are known to be unreliable in indoor environments, we use only 3D accelerometer and 3D gyroscope readings. Compensation of integration drift in the horizontal plane is achieved by estimating the gyroscope biases from automatically detected initial rest phases. For the estimation of sensor orientations, both a smoothing algorithm and a filtering algorithm are presented. From these orientations, we determine three-dimensional joint angles between the thighs and the pelvis and between the pelvis and the lumbar region. We compare the orientations and joint angles to measurements of an optical motion tracking system that tracks each skin-mounted sensor by means of reflective markers. Eight subjects perform a neutral initial pose, then flexion/extension, lateral flexion, and rotation of the trunk. The root mean square deviation between inertial and optical angles is about one degree for angles in the frontal and sagittal plane and about two degrees for angles in the transverse plane (both values averaged over all trials). We choose five features that characterize the initial pose and the three motions. Interindividual differences of all features are found to be clearly larger than the observed measurement deviations. These results indicate that the proposed inertial sensor-based method is a promising tool for lower back motion assessment.

Index Terms—Inertial measurement units, joint angle estimation, human motion analysis, low back pain, back motion assessment, avoid magnetometers, validation against optical motion capture, drift correction.

I. INTRODUCTION

Low back pain (LBP) is the leading cause of activity limitation and work absence throughout much of the world, and it causes an enormous economic burden on individuals, families, communities, industry and governments [1]. Proper diagnosis and effective therapies are therefore of major importance. Objective assessment of the movement impairments due to LBP has the potential to aid clinical assessment and provide important treatment targets [2]. Utilizing optical marker-based systems for motion tracking is the current gold standard. These systems possess a high accuracy but they are stationary, their set-up is complex and the acquisition costs are high. In contrast, wearable inertial measurement units (IMUs) facilitate simple and ambulatory motion tracking at much lower costs. They have successfully been used in a multitude of biomedical applications ranging from gait analysis [3], [4] and assessment

of muscle spasticity [5] to biofeedback for balance improvement [6] and realtime feedback control of neuroprostheses for paretic limbs [7]. In the present work we address the problem of using a wireless IMU network to estimate and assess motion of the lower back, as illustrated in Figure 1.

IMUs typically measure acceleration, angular rate and the magnetic field vector in their own three-dimensional intrinsic coordinate system. The available 9D data can be processed by a sensor fusion algorithm to calculate the sensor orientation relative to a global fixed coordinate system. In a nutshell, the sensor orientation is calculated by integrating the measured angular rate and by using accelerometer and magnetometer readings to correct the integration drift that results from non-zero gyroscope bias and noise. Here, accelerometer readings can correct for integration drift in the vertical plane (inclination), while magnetometer readings can correct for integration drift in the horizontal plane (heading). Specifically the latter is challenging in practice, since many indoor environments include ferromagnetic material and electromagnetic fields, which distort the local magnetic field measurements [8]. Despite recent advances, the effect of these disturbances can not be eliminated completely [9]. Because of this, we propose a method that uses only accelerometer and gyroscope readings.

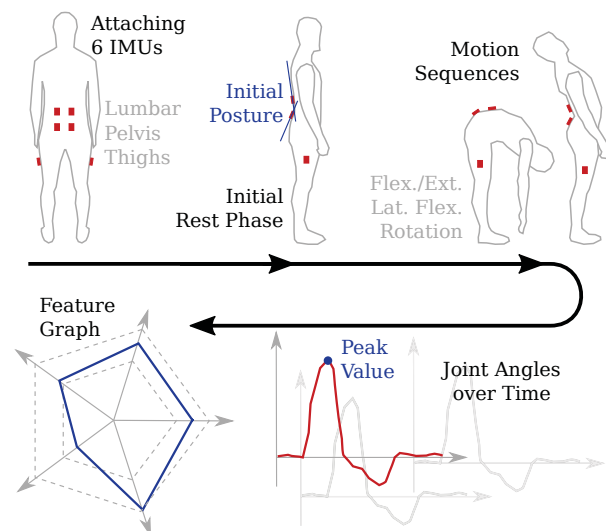


Fig. 1. Concept of IMU-based lower back motion assessment.

In recent years, several other researchers have refrained from using magnetometer readings in indoor applications. They typically compensate integration drift by exploiting kinematic constraints. For instance, a recent optimization-based method for inertial motion capture utilizes the constraints of biomechanical joints, while the magnetometer data is only used in the initialization process [10]. The method was successfully applied to estimate the motion of different segments of the human body. Another recent approach uses the joint constraints of a robot arm and zero-velocity corrections and yields a maximum heading error of about 8° over a time period of 15 minutes [11]. For the human knee and elbow, accuracies of about 3° have been obtained by exploiting the respective kinematic constraints [12], [13]. With respect to spine motion analysis, a constraint-based approach was used to track the joint positions of the thoracic and lumbar vertebrae with errors between one and seven centimeters [14]. All these magnetometer-free approaches rely on biomechanical constraints, and either require parameters determined by manual measurements, which depend on human accuracy, or require sufficient excitation of the degrees of freedom of the joints.

Because we are interested in assessing back motion of a large number of subjects with very individual body dimensions and ranges of motions, manual measurements are not practical and sufficient excitation can not be assumed. We therefore propose a different approach for eliminating integration drift in the horizontal plane: The user is asked to stand still at the beginning of each trial. This initial rest phase can be used to estimate the gyroscope bias and the initial sensor inclinations. Since the subjects are not completely stationary during this rest phase, we design an algorithm that carefully selects a subset of the measured samples for gyroscope bias estimation. We use this sample selection procedure in combination with two different sensor fusion algorithms – a filtering and a smoothing approach. The practical usefulness of the methods is demonstrated in experiments with eight subjects performing sequences of back motions that are typical in low back pain assessment.

II. PROBLEM FORMULATION

When analyzing back motion to assess low back pain, physicians are typically interested in the posture of the back when the subject is asked to stand straight (neutral pose) and in the motion, particularly the range of motion, of the lower back and the pelvis during single-axis motions (flexion, lateral flexion, and rotation) of the trunk [2]. In the present study, we want to quantify these motions and the neutral pose objectively using wireless IMUs, which are attached to the thighs, pelvis, and lumbar region of the spine, as illustrated in Figure 2. The subjects are asked to stand still in a neutral pose for at least seven seconds (i.e. the aforementioned rest phase) and then to perform either of the following three motion sequences:

- 1) A maximum flexion of the back followed by a maximum extension of the back and a return to the neutral pose, then a repetition of the flexion and the extension.



Fig. 2. Illustration of motion sequences, IMU attachment on subject and central IMUs: (a) Flexion/extension (b) Lateral flexion (c) Rotation (d) Attachment of the six IMUs on subject (e) Approximated central orientations, illustrated by central IMUs.

- 2) A maximum lateral flexion of the back to the right, then a maximum lateral flexion to the left, then return to neutral pose, finally a repetition of the lateral flexion to both sides.
- 3) An analogous sequence of back rotations around the vertical axis, again to the right and left, and with a repetition.

These three motion sequences are illustrated in Figure 2a–c, respectively. To estimate the relevant angles, in Section III, we propose methods to obtain accurate orientation estimates from the inertial sensors. This provides information about the orientation of each sensor at each time instance. In Section IV we subsequently describe how these sensor orientations are used to determine meaningful parameters describing the individual subject's initial pose and range of motion of the lower back.

III. METHODS

In this section, we propose two different methods to estimate the orientation of six wireless IMUs (Musclelab, Ergosteg Innovation A.S., Norway) that are attached to the left (L) and right (R) side of the lumbar region (L), the pelvis (P) and the thighs (T) as illustrated in Figure 2d.

The subjects perform the three different motion sequences described in Section II. Each of the six IMUs measures accelerations $\mathbf{a}(t) \in \mathbb{R}^3$ and angular rates $\mathbf{g}(t) \in \mathbb{R}^3$ with

Alg 1: Back Motion Assessment Algorithm

Input: Gyroscope and accelerometer measurements $\mathbf{g}(t)$ and $\mathbf{a}(t)$ from the six sensors that are attached to the lumbar region (L), the pelvis (P) and the thighs (T).

Output: Joint angle of the virtual central orientation of the lumbar region and the pelvis L_C/P_C and five characteristic features of motion.

1: **Rest phase sample selection:**

- Determine the rest phase using the gyroscope data from the left lumbar sensor.
- For each of the six sensors, detect the small motions during this rest phase and return the samples of low activity and an adapted vector of gyroscope measurements.

2: **Orientation estimation:** Compute the orientations for each of the six sensors using either the filtering algorithm described in Section III-B or the smoothing algorithm presented in Section III-C.

3: **Calculating meaningful motion parameters:**

- Use the orientation estimates from the left and the right sensors placed on the pelvis and lumbar region to compute virtual central orientations L_C and P_C .
- Use the virtual central orientation to compute the joint angle L_C/P_C .
- Use the joint angle L_C/P_C to compute five characteristic features of motion.

a frequency of 200 Hz for $t \in [t_s, t_e]$, where $t_s \in \mathbb{R}^+$ and $t_e \in \mathbb{R}^+$ are the initial and final times of the measurement. Since the magnetic field vector is unreliable in indoor environments, it is not utilized for the correction of the heading. Instead, the gyroscopes bias is compensated by bias estimation and correction based on data of the rest phase. The rest phase detection algorithm is described in Section III-A. Subsequently, we will explain how the result of the algorithm is used to estimate the IMU orientations and then determine features that characterize the motions performed by a subject. An overview of the entire method is given in Algorithm 1.

A. Rest Phase Sample Selection

Each data set can be separated into an initial rest phase, during which the subject is asked to stand still, and a subsequent motion phase during which the described motion sequence is performed. To determine the gyroscope bias as accurately as possible from samples of low activity, we present a two-step heuristic algorithm. In a first step, the transition between rest phase and motion phase is detected. Subsequently, the rest phase data is analyzed by a second algorithm, which finds and eliminates time periods within the rest phase during which the subject was not standing still enough.

The first algorithm, which detects the motion onset, utilizes the left lumbar sensor L_L as an indicator for rest versus

motion, since the lumbar region is expected to be relatively steady during sitting and standing but moves notably during each motion sequence. The Euclidean norm of the gyroscope measurements $\mathbf{g}(t)$ of that sensor is denoted by $g(t)$ and used to distinguish the rest phase from the motion phase as follows:

- 1) First, the norm of the gyroscope measurements $g(t)$ is filtered by a zero-phase moving average filter with window size of one second leading to $g_{f1}(t)$.
- 2) Define the first-four-second mean of $g_{f1}(t)$ as

$$\lambda_0 := \text{avg}_{t \in [t_s, t_s+4s]} g_{f1}(t), \quad (1)$$

representing the approximate level of activity of the initial rest phase. This level of activity is assumed to be much smaller than the maximum activity during the actual motion sequence. Define a high-activity threshold λ_{high} at 20% between that maximum and λ_0 :

$$\lambda_{\text{high}} := 0.2 \left(\max_{t \in [t_s, t_e]} (g_{f1}(t)) - \lambda_0 \right) + \lambda_0 \quad (2)$$

- 3) Determine the first time instant $t_{\text{high}} \in [t_s, t_e]$ at which $g_{f1}(t)$ exceeds the threshold λ_{high} and find the largest value $t_1 < t_{\text{high}}$ for which

$$\text{avg}_{t \in [t_1-2s, t_1]} g_{f1}(t) < 2\lambda_0. \quad (3)$$

This is to assure that the time interval $[t_1 - 2s, t_1]$ is the last sufficiently long period of calm motion before the onset of high activity.

- 4) Finally, return the time instant of the smallest $g_{f1}(t)$ in that two-second interval as the time t_{mo} of motion onset

$$t_{\text{mo}} := \arg \min_{t \in [t_1-2s, t_1]} g_{f1}(t). \quad (4)$$

These four steps are illustrated in the left subfigures of Figure 4 using an example data set. The top left plot shows $g(t)$ as a gray thin line in the background and $g_{f1}(t)$ as a blue thick line in the foreground. The maximum activity $\max_{t \in [t_s, t_e]} (g_{f1}(t))$ is indicated by a red dot. The high-activity threshold λ_{high} is marked by a horizontal red line, and the horizontal black line indicates $2\lambda_0$. The lower left plot shows a close-up of the upper left plot. Therein, the time interval $[t_1 - 2s, t_1]$ is marked by black brackets, and the red dot represents the moment of smallest value in that time interval, i.e. the motion onset t_{mo} .

If the subject would not be moving during the rest phase, the samples from the rest phase could directly be used to calculate the gyroscope bias of each of the sensors by computing the mean of the angular rate vector over that interval. In practice, however, the subjects do not stand perfectly still. They may wobble, jerk or tremble slightly during the rest phase. Thus, intervals of such *small motions* have to be determined and handled for each of the sensors. To this end, the following procedure is applied to the gyroscope measurements from the rest phase interval $t \in [t_s, t_{\text{mo}}]$ from each of the sensors:

- 1) A zero-phase moving average with window size of 0.25 s is applied to the angular rates $\mathbf{g}(t)$, yielding $\mathbf{g}_{f2}(t)$, and to the norm $g(t)$, yielding $g_{f2}(t)$.

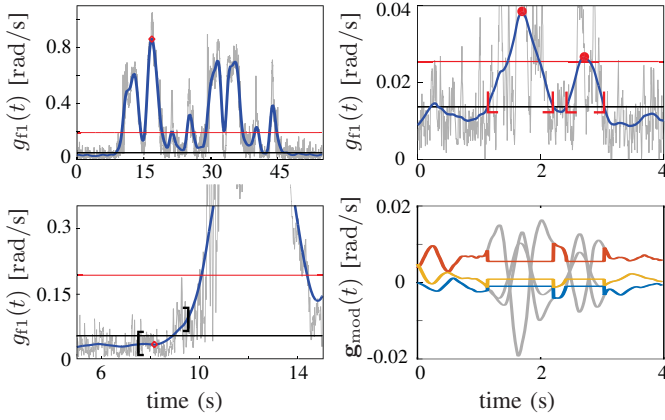


Fig. 4. Example data for motion onset detection and bias estimation. *Left:* Lowpass-filtered angular rate norm and threshold for the entire motion sequence and close-up on the motion onset. *Right:* Minor movements during rest phase are detected and the angular rates are adjusted (raw data in gray).

- 2) Introduce the initial set of high-activity indices as $H = \emptyset$ and the mean of $g_{f2}(t)$ over $[t_s, t_{mo}]$ as λ_{rest} .
- 3) To fill the set H with high-activity indices, the following steps are applied in a loop
 - a) If $\max_{t \in [t_s, t_{mo}]} g_{f2}(t) < 1.9 \lambda_{rest}$, i.e. if even the largest *small motion* during rest phase is negligible, then exit the loop.
 - b) Else, add the time instant of that maximum as well as all preceding and following time indices for which $g_{f2}(t) > \lambda_{rest}$ holds to the set H . Thereby, H contains the entire time interval associated with the *small motion* that occurred during rest phase.
 - c) Replace the values of $g_{f2}(t)$ at all aforementioned indices with λ_{rest} and repeat from 3a) with the modified signal $g_{f2}(t)$, $t \in [t_s, t_{mo}]$, until all remaining *small motions* are negligible.
- 4) The sample values $g_{f2}(t)$, $t \in H$, are replaced by the mean vector of $g_{f2}(t)$, $t \in [t_s, t_{mo}]$, yielding the modified gyroscope rest phase data $g_{mod}(t)$, $t \in [t_s, t_{mo}]$.

Figure 4 illustrates the detection and elimination of *small-motion* data using an example data set. The right upper plot shows $g(t)$ as a thin gray line in the background, $g_{f2}(t)$ as a thick blue line in the foreground, and λ_{rest} as a thin black horizontal line. Red dots indicate the maximum values of $g_{f2}(t)$ for two subsequent loops of step 3a). Both are larger than the threshold $1.9\lambda_{rest}$ that is marked by a red horizontal line. Red brackets enclose the sampling indices that are added to the set H as described in step 3b). The right lower subplot shows the original angular rates $g_{f2}(t)$ in gray and the modified signals $g_{mod}(t)$ as colored lines, in which the values at sample indices belonging to H have been replaced by the average of $g_{f2}(t)$ over the entire rest interval.

By means of the two algorithms described above, we obtain a rest phase as well as modified gyroscope rest data that no longer contains small-motion data. If the rest phase is long enough we can obtain accurate estimates of the gyroscope

biases. In the present data the duration of each subject's rest phase is at least seven seconds. However, it is an important research question whether shorter rest phases can be used. To facilitate investigation of this question, we introduce the parameter $\Delta t_{rest} \leq 7$ s, and we restrict our analysis to the time interval $t \in [t_{mo} - \Delta t_{rest}, t_e]$ in the following, i.e. all data with $t < t_{mo} - \Delta t_{rest}$ is disregarded.

B. Filtering Algorithm

We estimate the bias of each gyroscope by averaging the modified gyroscope rest data $g_{mod}(t)$ over the time interval $[t_{mo} - \Delta t_{rest}, t_{mo}]$. This bias estimate is then subtracted from the original gyroscope readings to obtain almost bias-free angular rates. We employ a recently developed realtime sensor fusion algorithm [9] that fuses these angular rates with the accelerometer readings to determine the quaternions $q_{L_L}, q_{L_R}, q_{P_L}, q_{P_R}, q_{T_L}, q_{T_R}$ that represent the orientations of all six IMUs with respect to a common inertial frame. The core elements of that algorithm are a gyroscope-based prediction, an accelerometer-based correction and a magnetometer-based correction, which is omitted in the current application. The gyroscope-based prediction is a pure strapdown integration of the measured angular rates. The accelerometer-based correction is based on an analytical solution of the sensor fusion problem, i.e. four-dimensional spherical linear interpolation between the predicted quaternion and the geometrically nearest quaternion that agrees with the current accelerometer reading. The algorithm is parametrized in a way that allows the user to choose the time constant and aggressiveness (overshoot) with which the algorithm balances between integration drift compensation and rejection of disturbances caused by velocity changes. A more detailed description is given in [9].

Due to the absence of magnetic field measurements, the initial heading of the sensors cannot be determined by the sensor fusion algorithm. Instead, we exploit the known sensor-to-segment orientation and initial pose. The IMUs at the lumbar and pelvic region are attached such that, at the initial neutral pose of the subject, the lower edge of the housing, i.e. the x-axis of the intrinsic measurement frame, is aligned with the mediolateral axis of the body. Likewise, the IMUs at the thighs are attached such that the frontal housing surface, i.e. the x-y-plane of the intrinsic measurement frame is orthogonal to the mediolateral axis of the body. This immediately determines the heading of all sensors at initial pose. From the moment of motion onset t_{mo} the heading is determined by the sensor fusion algorithm, i.e. by strapdown integration of the almost bias-free angular rates.

C. Smoothing Algorithm

Alternatively, the orientation of the different sensors can be estimated using a smoothing algorithm. We use a slightly different model from the one used in Section III-B and use the samples of the rest phase determined from the procedure described in Section III-A to indicate whether the angular velocity at time t is equal to zero. Let S be the set of all sampling indices in the time interval $t \in [t_{mo} - \Delta t_{rest}, t_{mo}]$,

and recall that the subset $H \subset S$, contains all indices with *small motions*.

We model the true angular rate $\mathbf{g}_{\text{true}}(t)$ of each sensor to be zero for $t \in S \setminus H$ and the gyroscope measurements $\mathbf{g}(t)$ to be equal to

$$\mathbf{g}(t) = \begin{cases} \mathbf{g}_{\text{true}}(t) + \mathbf{b}_g + \mathbf{e}_g(t), & t \notin S \setminus H \quad (5a) \\ \mathbf{b}_g + \mathbf{e}_g(t), & t \in S \setminus H \quad (5b) \end{cases}$$

where \mathbf{b}_g denotes the gyroscope bias, which is assumed to be constant for the timespan of each trial, and the gyroscope noise $\mathbf{e}_g(t)$ is modeled as white Gaussian noise $\mathbf{e}_g(t) \sim \mathcal{N}(0, \sigma_g^2 \mathcal{I}_3)$. Similar to the filtering approach, the accelerometer measurements $\mathbf{a}(t)$ are assumed to measure the Earth's gravity in their local sensor frame and the initial heading at time $t_{\text{mo}} - \Delta t_{\text{rest}}$ is initialized using ground truth data.

Let $\hat{t} = 1, \dots, N$ be the discrete time index of all sampling instants $t \in [t_{\text{mo}} - \Delta t_{\text{rest}}, t_e]$. For each sensor, our smoothing implementation computes a *maximum a posteriori estimate* of the orientation at all these time instants by solving the following optimization problem

$$\arg \min_{\mathbf{x}_{1:N}, \mathbf{b}_g} \left(\underbrace{-\log p(\mathbf{x}_1)}_{\text{Initialization}} - \sum_{\hat{t}=2}^N \log p(\mathbf{x}_{\hat{t}} | \mathbf{x}_{\hat{t}-1}, \mathbf{g}(\hat{t})) \right. \\ \left. - \underbrace{\sum_{\hat{t}=1}^N \log p(\mathbf{a}(\hat{t}) | \mathbf{x}_{\hat{t}})}_{\text{Accelerometer measurement model}} \right). \quad (6)$$

where the state vector \mathbf{x} denotes a parametrization of the orientation of the sensor, and its lower index has the following meaning: $\mathbf{x}_{1:N}$ denotes the orientations at all $t \in [t_{\text{mo}} - \Delta t_{\text{rest}}, t_e]$, \mathbf{x}_1 denotes the orientation at $t_{\text{mo}} - \Delta t_{\text{rest}}$, $\mathbf{x}_{\hat{t}}$ denotes the orientation at some sampling instant, and $\mathbf{x}_{\hat{t}-1}$ denotes the value at the preceding sampling instant.

Assuming that the noise on the initialization is $\mathbf{e}_{\text{init}} \sim \mathcal{N}(0, \Sigma_{\text{init}})$ and the accelerometer measurement noise is $\mathbf{e}_a(t) \sim \mathcal{N}(0, \Sigma_a)$, (6) reduces to a weighted least squares problem

$$\arg \min_{\mathbf{x}_{1:N}, \mathbf{b}_g} \|\mathbf{e}_{\text{init}}\|_{\Sigma_{\text{init}}^{-1}}^2 + \sum_{\hat{t}=2}^N \|\mathbf{e}_g(\hat{t})\|_{\Sigma_g^{-1}}^2 + \sum_{\hat{t}=1}^N \|\mathbf{e}_a(\hat{t})\|_{\Sigma_a^{-1}}^2. \quad (7)$$

For more details on the implementation of the algorithm and the parametrization of the orientation, we refer the reader to [15]. One of the main differences between filtering and smoothing approaches is that filtering computes the estimates given the measurements up to the current time step while smoothing uses all available measurements. Another notable difference between the two approaches in our case is that the smoothing approach explicitly estimates the gyroscope bias using not only the samples from the rest phase but also all other samples. It is therefore able to adjust the estimates using any further information that is present in the data.

IV. CALCULATING MEANINGFUL MOTION PARAMETERS FROM SENSOR ORIENTATIONS

For the pelvis and the lumbar region, a virtual central orientation is calculated from the orientations of the right and the left sensor by quaternion interpolation. In Figure 2e these orientations are illustrated with their shorthand notations L_C and P_C . For each pair of orientations of neighboring body segments, we calculate the relative orientation. For example, with \otimes denoting quaternion multiplication, the quaternion

$$q_{L_L/P_L} = (q_{P_L})^{-1} \otimes q_{L_L} \quad (8)$$

describes the orientation of the sensor placed on the right side of the lumbar region (L_L) relative to the sensor placed on the left side of the pelvis (P_L). To describe only the motion with respect to the initial pose, we define the initial-reset quaternions

$$q_{A/B, \text{ir}}(t) = (q_{A/B}(t_{\text{mo}} - \Delta t_{\text{rest}}))^{-1} \otimes q_{A/B}(t), \quad (9)$$

where A and B are any neighboring body segments. We can use (9) to determine the joint angles between L_L/P_L , L_R/P_R , P_L/T_L , and P_R/T_R and use these angles to analyze the motion in detail. However, in the current contribution, our focus is on L_C/P_C , i.e. on the relative motion of the virtual central lumbar IMU with respect to the virtual central pelvis IMU. The initial-reset quaternions are decomposed into three Euler angles representing flexion/extension, lateral flexion and rotation. For each motion sequence, one of these angles is dominant: flexion/extension for the first motion sequence, lateral flexion for the second and rotation for the third motion sequence.

The described method yields measurement curves of a large number of joint angles. For a practical assessment of the subjects' motions, we propose the following characteristic features: The first two features are the inclination angles of L_C and P_C at $t = t_{\text{mo}} - \Delta t_{\text{rest}}$. We determine these values for the first two motion sequences (flexion/extension and lateral flexion), and denote the mean inclination angles of L_C and P_C by L_C^{IPI} and P_C^{IPI} , respectively. Figure 5 illustrates the relevance of these parameters for pathological back postures. Note that the third motion sequence is performed sitting and therefore does not provide useful information about these angles.

The third to fifth feature are the largest positive values of the main angles of $q_{L_C/P_C, \text{ir}}$ reached during the second repetition of each motion sequence. Note that the decision to consider only the positive peak is for the sake of simplicity – in clinical practice both peaks might be of interest. In other words, the third to fifth feature are defined as

- the largest flexion/extension angle from the first motion sequence denoted by “FE Peak”,
- the largest lateral flexion angle from the second motion sequence denoted by “LF Peak”,
- the largest rotation angle from the third motion sequence denoted by “RT Peak”.

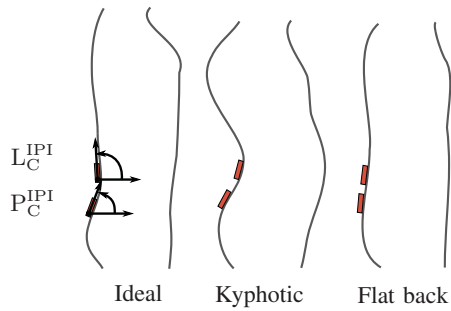


Fig. 5. Exemplary postures in grey with virtual central orientations symbolized by red boxes. The definition of L_C^{IPI} and P_C^{IPI} is illustrated utilizing the ideal posture example.

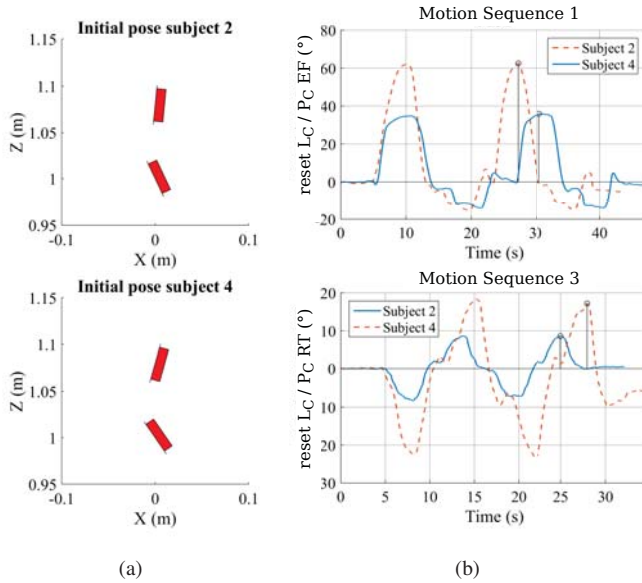


Fig. 6. Exemplary evaluation results for two subjects. (a) 2D illustration of L_C and P_C initial-pose inclination (IPI). (b) Main joint angles of L_C/P_C for Motion Sequence 1 and 3. Initial reset (9) is applied before calculating the angles, i.e. only motion with respect to initial pose is presented.

In Figure 6 the utilization of the proposed features is illustrated by comparing two subjects regarding the initial pose and the main joint angle of reset L_C/P_C for the first third motion sequences. The FE Peak values and RT Peak values are indicated by stems.

V. VALIDATION OF MEASUREMENT ACCURACY

To validate the method, it is applied to 8 subjects with average and standard deviation weight of 68 ± 13 kg, height 172 ± 8 centimeters and age 30 ± 4 . Ground-truth reference orientations are obtained from a marker-based optical system (Vicon Motion Systems Ltd., UK) that tracks the three-dimensional marker positions at 500 Hz. For this purpose, a very lightweight and rigid marker tripod is built and attached to each IMU, as shown in Figure 7(a). The tripods are designed and attached in a way that minimizes overlay between markers of pelvis/lumbar IMUs. Since the axes of the marker tripods do not coincide with the local IMU coordinate axes and

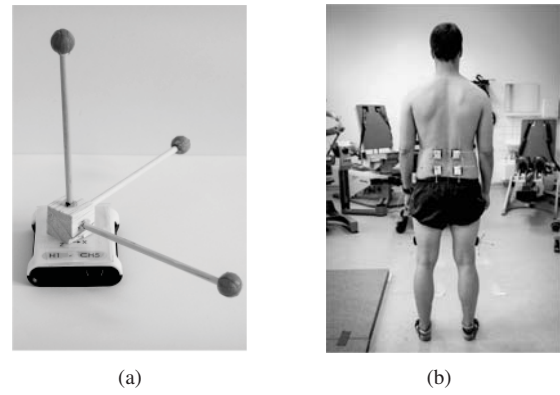


Fig. 7. Hardware setup for validation: (a) IMU with rigid, lightweight optical-marker tripod. (b) IMUs with marker tripods attached to subject.

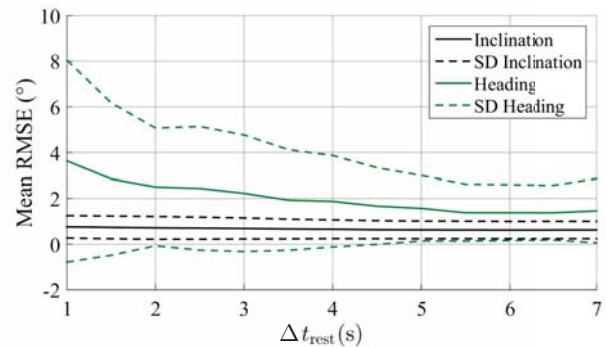


Fig. 8. Influence of initial rest duration Δt_{rest} on tracking error ($\text{RMSE} \pm \text{SD}$ of inclination and heading angle, averaged over all trials, subjects, sensors).

since the optical coordinate system does not coincide with the global fixed coordinate system of the IMUs, we need to account for these offsets before the measurements of both systems can be compared. The offsets are removed using a simple calibration sequence that is performed by each subject prior to the actual trials [16]. Note that this procedure is only required for validation against the optical system but not for inertial back motion assessment itself. Once the local and global axes of both systems agree, we can compare the orientations $q_{L_L}, q_{L_R}, q_{P_L}, \dots$ measured by the inertial and the optical systems. To analyze how successful the rest phase sample selection was, we transform the quaternions into the global fixed frame and decompose them into an inclination part and a heading part. Recall that the rest phase interval is defined as $t \in [t_{\text{mo}} - \Delta t_{\text{rest}}, t_{\text{mo}}]$, where Δt_{rest} is some duration less than or equal to seven seconds. We now investigate the influence of this rest phase duration on the average inclination and heading errors (averaged over all subjects, motion sequences and sensors). Figure 8 shows that longer rest phase durations lead to smaller tracking errors. The approximately optimal choice is $\Delta t_{\text{rest}} = 5.5$ s, which is used throughout the remainder of this paper. Figure 9 illustrates the difference between optical and inertial measurements for the first repetition of flexion/extension in the first motion sequence

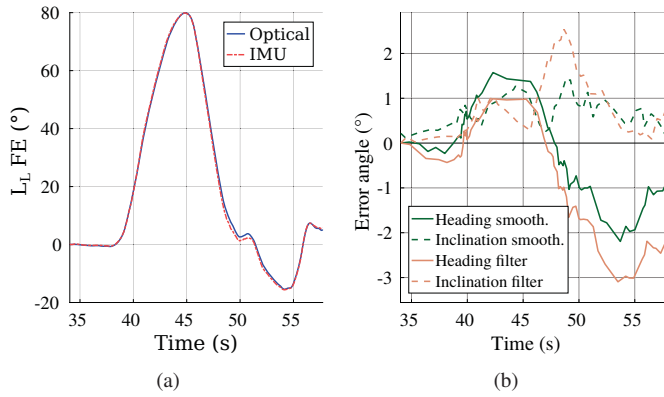


Fig. 9. Comparison of L_L FE angle for first flexion/extension of Motion Sequence 1 performed by Subject 1. (a) L_L FE of both systems. (b) Corresponding error angles of heading and inclination.

of Subject 1. The right subplot reveals that this motion was captured slightly better by the smoothing algorithm than by the filtering algorithm (two degrees maximum deviation instead of three).

The summarized validation results, i.e. root-mean-square deviations for each of the sensors averaged over all subjects and motion sequences, are listed in Table I. The data reveals that the inclination is measured more accurately than the heading. However, both quantities remain close to the reference measurements. For the smoothing method, the average RMSE of the heading is below two degrees for all sensors (body segments).

TABLE I
RMSE BETWEEN INERTIAL AND OPTICAL ORIENTATIONS – MEAN, STD. DEVIATION AND MAXIMUM OVER ALL SUBJECTS AND TRIALS.

Sensor	RMSE of sensor <u>inclination</u> (°)			
	Filtering method		Smoothing method	
	Mean \pm SD	Max	Mean \pm SD	Max
L_L	1.0 \pm 0.6	1.9	0.8 \pm 0.5	1.7
L_R	0.8 \pm 0.3	1.6	0.7 \pm 0.3	1.3
P_L	0.5 \pm 0.2	0.9	0.5 \pm 0.3	1.2
P_R	0.6 \pm 0.3	1.4	0.6 \pm 0.3	1.4
T_L	0.4 \pm 0.2	0.8	0.4 \pm 0.2	0.9
T_R	0.5 \pm 0.1	0.7	0.5 \pm 0.1	0.7

Sensor	RMSE of sensor <u>heading</u> (°)			
	Filtering method		Smoothing method	
	Mean \pm SD	Max	Mean \pm SD	Max
L_L	2.5 \pm 1.8	6	1.7 \pm 1.4	5.4
L_R	2.1 \pm 1.6	6.7	1.7 \pm 1.2	4.9
P_L	0.9 \pm 0.7	3.4	1.0 \pm 0.8	2.8
P_R	0.9 \pm 0.7	3.3	0.9 \pm 0.6	2.6
T_L	1.0 \pm 1.3	6.3	0.8 \pm 0.8	3.1
T_R	1.4 \pm 1.0	4.9	1.3 \pm 0.9	4.9

The joint angles are validated by comparing the main angles for each of the three motion sequences. The results are summarized in Table II by the mean RMSE over all subjects. The average RMSE is below one degree for most and below two degrees for all joint angles and motion sequences.

TABLE II
DISAGREEMENT BETWEEN THE MAIN JOINT ANGLES FROM THE OPTICAL METHOD AND THE INERTIAL SMOOTHING METHOD.

Orientation	RMSE of main angle (°)		
	MS1 (FE)	MS2 (LF)	MS3 (RT)
	Mean \pm SD	Mean \pm SD	Mean \pm SD
reset L_L/P_L	0.9 \pm 0.2	0.7 \pm 0.5	1.7 \pm 2.1
reset L_R/P_R	0.7 \pm 0.2	1.1 \pm 0.9	0.7 \pm 0.6
reset P_L/T_L	0.5 \pm 0.2	1.0 \pm 1.0	0.6 \pm 0.3
reset P_R/T_R	0.6 \pm 0.2	0.6 \pm 0.3	2.0 \pm 0.2

TABLE III
INITIAL POSE AND PEAK ANGLES FOR ALL SUBJECTS.

Subject	Initial pose angles (°)		Peak angles (°)		
	L_C^{IPI}	P_C^{IPI}	FE Peak	LF Peak	RT Peak
1	99.4	65.1	46.3	9.1	17.1
2	95.6	64.9	35.8	11.1	8.6
3	94.3	62.0	39.3	16.1	16.3
4	105.6	55.5	62.6	11.6	16.3
5	87.3	68.9	40.2	16.0	16.2
6	91.8	65.2	53.1	13.1	15.3
7	86.1	62.1	33.4	16.2	8.2
8	94.9	59.7	47.0	11.7	11.9

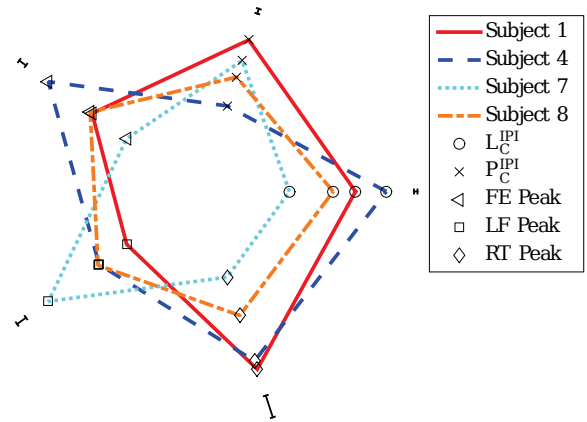


Fig. 10. Radar chart of the initial pose and peak angles for four subjects. Black bars represent the magnitude of the mean tracking error for each angle. For each category, the interindividual differences are larger than these errors.

To quantify interindividual changes in the proposed initial pose and peak angle features, we compare these quantities for all subjects in Table III. Figure 10 shows the individual values of four of the subjects as corners of a pentagon with black bars representing the average measurement error of the angle that the feature is based on, respectively.¹

VI. DISCUSSION OF RESULTS

The proposed methods for bias compensation and sensor orientation estimation achieve heading RMSE values that vary between 0.9° and at most 2.5° for the filtering approach and

¹Due to missing marker position data for sensor P_L in MS2 of subject 5, the results for P_L heading and inclination error (Table I), reset P_L/T_L MS2 main angle RMSE and the mean error of LF Peak in Figure 10 are calculated based on one less ground-truth data set than for the other listed errors.

between 0.8° and at most 1.7° for the smoothing approach (see Table I), which is approximately twice as large as the inclination errors. One potential explanation is found in Figure 9(b). The heading error increases for about five seconds and then decreases to negative values for about ten seconds, which indicates that the bias is time-variant.

Table II shows that the different accuracy levels for inclination and heading lead to different accuracies in the main angles of the motion sequences. The largest RMSE values of Motion Sequence 3 (rotation) are approximately twice as large as those of Motion Sequence 1 and 2 (flexion/extension and lateral flexion), respectively. However, the mean is at most 2° for all joint angles. More important than these numbers themselves is the question whether they are small enough to objectively quantify differences in motion performance between subjects. Figure 10 illustrates that the differences in the proposed characteristic feature values between all subjects are clearly larger than the respective measurement error. Especially the inclination angles and the peak values of Motion Sequence 1 and 2 show variations across the subjects that are several times larger than the respective RMSE values.

VII. CONCLUSION

We proposed a method for objective ambulatory assessment of back motions by 6D inertial measurement units. By only relying on angular rate and acceleration readings we assured that the proposed method works in arbitrary indoor environments regardless of the homogeneity of the local magnetic field. To facilitate gyroscope bias estimation, the subject is required to sit or stand calmly before performing the motion sequence of interest. Small motions, which might occur during this initial rest phase, are automatically detected and compensated. Experimental validation revealed that the proposed methods are precise enough to allow quantification of inter-individual changes in the performance of back motions. If pathologies affect the way that people perform back motions, then these changes will most likely be observable by the proposed methods. Progress monitoring for assessment of treatment effects as well as identification of high-risk individuals are only two potential use cases.

In future work the measurement accuracy could further be improved by taking time-variant bias models into account. When employing the method in larger studies, interrater and intrarater reliability will be examined, i.e. the reliability of the method with respect to variations in repeated measurements performed by one and the same examiner as well as with respect to variations in measurements performed by different examiners. Finally, it should be noted that the proposed methods are not limited to back motion analysis but will be used in the context of motion analysis for other body segments and applications.

ACKNOWLEDGMENTS

The authors would like to thank all subjects who volunteered for the motion capture trials.

This research was financially supported by the EPSRC grant *Autonomous behaviour and learning in an uncertain world* (Grant number: EP/J012300/1) and by the German Federal Institute of Sport Science under the auspices of *MiSpEx – the National Research Network for Medicine in Spine Exercise* (Grant number: BISp IIA1-080102A/11-14).

REFERENCES

- [1] B. Duthey, "Background paper 6.24 – low back pain." in *Priority Medicines for Europe and the World – 2013 Update. Background Paper 6 – Priority Diseases and Reasons for Inclusion*. World Health Organization (WHO), March 2013.
- [2] E. Papi, A. M. Bull, and A. H. McGregor, "Is there evidence to use kinematic/kinetic measures clinically in low back pain patients? a systematic review," *Clinical Biomechanics*, vol. 55, pp. 53 – 64, 2018.
- [3] B. Mariani, C. Hskovec, S. Rochat, J. Pender, and A. Kamiar, "3D gait assessment in young and elderly subjects using foot-worn inertial sensors," *Journal of Biomechanics*, vol. 43, no. 15, pp. 2999–3006, 2010.
- [4] P. Müller, T. Seel, and T. Schauer, "Experimental evaluation of a novel inertial sensor based realtime gait phase detection algorithm," in *Proceedings of the 5th European Conference on Technically Assisted Rehabilitation (TAR)*, Berlin, Germany, 2015.
- [5] J. van den Noort, V. Scholtes, and J. Harlaar, "Evaluation of clinical spasticity assessment in cerebral palsy using inertial sensors," *Gait & Posture*, vol. 30, no. 2, pp. 138–143, 2009.
- [6] C. Z.-H. Ma, D. W.-C. Wong, W. K. Lam, A. H.-P. Wan, and W. C.-C. Lee, "Balance improvement effects of biofeedback systems with state-of-the-art wearable sensors: A systematic review," *Sensors*, vol. 16, no. 4, 2016.
- [7] T. Seel, C. Werner, and T. Schauer, "The adaptive drop foot stimulator – Multivariable learning control of foot pitch and roll motion in paretic gait," *Medical Engineering & Physics*, vol. 38, no. 11, pp. 1205–1213, 2016.
- [8] E. R. Bachmann, X. Yun, and C. W. Peterson, "An investigation of the effects of magnetic variations on inertial/magnetic orientation sensors," in *Proceedings of the IEEE International Conference on Robotics and Automation*, vol. 2, April 2004, pp. 1115–1122.
- [9] T. Seel and S. Ruppig, "Eliminating the effect of magnetic disturbances on the inclination estimates of inertial sensors," in *Proceedings of the 20th IFAC World Congress*, Toulouse, France, July 2017, pp. 8798–8803.
- [10] M. Kok, J. D. Hol, and T. B. Schön, "An optimization-based approach to human body motion capture using inertial sensors," in *Proceedings of the 19th IFAC World Congress*, vol. 47, no. 3, 2014, pp. 79–85.
- [11] M. El-Gohary and J. McNames, "Human joint angle estimation with inertial sensors and validation with a robot arm," *IEEE Transactions on Biomedical Engineering*, vol. 62, no. 7, pp. 1759–1767, July 2015.
- [12] D. Laidig, P. Müller, and T. Seel, "Automatic anatomical calibration for imu-based elbow angle measurement in disturbed magnetic fields," *Current Directions in Biomedical Engineering*, vol. 3, no. 2, pp. 167–170, 2017.
- [13] T. Seel, J. Raisch, and T. Schauer, "IMU-based joint angle measurement for gait analysis," *Sensors*, vol. 14, no. 4, pp. 6891–6909, 2014.
- [14] M. Miezal, B. Taetz, N. Schmitz, and G. Bleser, "Ambulatory inertial spinal tracking using constraints," in *Proceedings of the 9th International Conference on Body Area Networks*, London, United Kingdom, Sept.-Oct. 2014, pp. 131–134.
- [15] M. Kok, J. D. Hol, and T. B. Schön, "Using inertial sensors for position and orientation estimation," *Foundations and Trends on Signal Processing*, vol. 11, no. 1–2, pp. 1–153, 2017.
- [16] J. D. Hol, "Sensor fusion and calibration of inertial sensors, vision, ultra-wideband and GPS," Dissertation No. 1368, Linköping University, Linköping, Sweden, Jun. 2011.